Activation of stainless steel 316L anode for anion exchange membrane water electrolysis

S. Nuggehalli Sampathkumar [a],[1],[*], T.B. Ferriday [a],[b],[1], P.H. Middleton [a],[b], J. Van Herle [a]

[a] *Group of Energy Materials, Swiss Federal Institute of Technology, Lausanne, Rue de l'Industrie 17, Sion, 1951 Valais, Switzerland*
[b] *Department of Engineering Science, University of Agder, Jon Lilletunsvei 9, Grimstad, 4879 Agder, Norway*

ARTICLE INFO

ABSTRACT

The increased emphasis on renewable energy has resulted in a surge of R&D efforts into hydrogen and battery research. The intensive electrochemical environment surrounding the anodic oxygen evolution reaction (OER) has plagued both the activity and stability of the catalytic layer, substrate and porous transport layer, ultimately affecting both these industries. Herein, we report the benefits of potential cycling (PC) a 316L stainless steel felt porous transport layer (PTL) for use in anion exchange membrane water electrolysis. The PC increased surface roughness and created a $CrFe_5Ni_2-O_xH_y$ layer through the oxidation of iron as shown by SEM, EDS, XPS, XRD and Raman spectroscopy. Post-PC tests in a three-electrode setup reveal a $\approx 68\%$ decline in polarisation resistance, which is reflected in its performance when employed as an anode in an anion exchange membrane water electrolyser (AEMWE). Overall, potential cycling the PTL under anodic conditions resulted in an improved performance when tested in a AEMWE. Implementing this treatment on stainless steel anodes could be considered to achieve an improved AEMWE performance.

1. Introduction

The production of green hydrogen through water electrolysis has been largely implemented using proton exchange membrane water electrolysers (PEMWEs) and alkaline water electrolysers (AWEs) [1,2]. It is most common for PEMWEs to employ Nafion-based acidic membranes which can operate at high current densities catalysed by platinum group metal (PGM) catalysts for both the hydrogen (HER) and oxygen evolution reactions (OER). The AWE is an established technology whose dominion over the realm of water electrolysis spans over a hundred years [2]. AWE is still the industry standard, despite the intrinsic advantages offered by PEMWEs, such as higher current densities and slender cell designs [1,2]. The anion exchange membrane (AEM) has transported many of these advantages from the acidic realm to the alkaline realm, birthing the AEM water electrolyser (AEMWE) [1–3]. Naturally, a great amount of R&D experience can be transferred from traditional AWEs and PEMWEs to the novel AEMWE, however challenges and optimisation issues related to use of considerably diluted KOH electrolytes (1.0 M vs 6.89 M), thinner cell designs and complicated anionic ionomer/AEM chemistries [4] remain prior to wide-scale implementation of this technology [1,2].

It is particularly the anode side of all the aforementioned types of electrolysis that has been examined meticulously over the years due to the eminent overpotential associated with the four electron reaction [2,5]. Moreover, the use of substrates/porous transport layers (PTLs) is particularly widespread for the anode, as use of anode-side catalyst coated membranes has resulted in catalyst detachment [6]. The anode demands the use of a catalyst coated substrate (CCS), thus the stability and activity of these substrates is of great importance for their viability for long-term employment.

A variety of activation methods have been utilised for increasing both the activity and stability of the electrodes in alkaline electrolytes, including chronoamperometry (CA) [7,8] and potential cycling (PC) [7,9]. Potential cycling has been repeatedly used for activating an electrode by repeatedly oxidising and reducing the surface [9]. However the manner in which this treatment is undertaken has a great affect on the final outcome with respect to both performance and surface conditions. The effect of modifying solid stainless steel electrodes (SSEs) has been explored for traditional AWEs through both mechanical modification and acid washing [10]. The use of a specific activation procedure with a combination of CA (10 min at 1.53 E_{RHE}, 5 min at 0.93 E_{RHE}) and PC (5 mV s^{-1}, 0.93–1.93 E_{RHE}) was reported by Moureaux [7] et al.

which resulted in the creation a layer of nickel imbibing both corrosion resistance and OER-activity. Accelerated activation through ex-situ PC was determined as a more time-efficient procedure compared against in situ activation through constant OER.

Catalyst stability on a stainless steel substrate was challenged with potential cycling under very different conditions (1000 mV s^{-1}, 0.5–1.8 E$_{RHE}$, 20 000 cycles) by Todoroki *et* al. [11] in an electrolyte typical of traditional AWE (7.0 M KOH) [2]. The catalyst layer displayed resilience towards the harsh conditions in maintaining a fairly constant overpotential at 100 mA cm^{-2}, a slight increase in series resistance and a dramatic increase in activity related to the Ni(II)/Ni(III) redox couple.

A lot of recent literature lays emphasis on testing a solid SSE under conditions associated with traditional AWEs [7,10–12], with less emphasis on conditions relevant to the novel AEMWE [7,8,13]. Additionally, several publications focus on creating an active oxide layer from a solid SSE and ascertaining its activity and stability [11,13–15]. No attention has so far been directed at testing the activity and stability of a porous 316L stainless steel PTL as a support and relating the change in surface conditions to the resulting performance. This would quantify the degree to which the substrate influences the overall cell performance, and thereby further isolating any changes elicited by or in the catalyst layer. Finally, the magnitude of these effects has yet to be seen in a AEMWE, as all effects related to potential cycling measured in a standard three-electrode setup cannot be assumed to be transferable to a full cell.

Herein, we address the aforementioned gap in literature by investigating how potential cycling a stainless steel 316L felt (SSF) porous transport layer (PTL) in 1.0 M KOH at 25°C affects its resulting performance in an AEMWE. The SSF PTL was tested before and after anodic potential cycling in an efficient three-electrode setup, before the same electrode was employed as an anode in a single cell AEMWE. The performance of the AEMWE was monitored and analysed using linear sweep voltammetry (LSV) and electrochemical impedance spectroscopy (EIS), where the treated SSF PTL displayed increased current density. Surface conditions were characterised by SEM/EDS, XRD, Raman spectroscopy and XPS, exhibiting the increased performance could be attributed to a active and stable CrFe$_5$Ni$_2$-O$_x$H$_y$ layer.

2. Experimental

The stainless steel electrodes were tested utilising an in–house created three-electrode setup as shown in Fig. S1 and in–house created AEMWE cell. All experimental details are listed in the supplementary information.

3. Results & discussion

3.1. Microstructural characterisation and analysis

The surface of the 316L stainless steel felt was composed of hexag-

onal strands with 14–16 μm faces. The felt was affected by the potential cycling as shown by the scanning electron microscope (SEM) figures in Fig. 1, where the surface displays a greater degree of small crevices and pits due to localised corrosion, though the face size of the strands remained unchanged. Elemental mapping through energy dispersive X-ray spectroscopy (EDS) figures are shown in Fig. S2, which display a homogeneous distribution of elements for the pristine electrode, while post-potential cycling EDS spectra display an increase in oxygen located in the newly formed crevices.

The XPS analysis in Fig. 2 shows high-resolution spectra of the principal components of 316L stainless steel, namely nickel, iron and chromium before and after potential cycling. The initial spectra in Figs. 2a, 2c & 2e generally show a weaker signal compared against the spectra taken after potential cycling shown in Figs. 2b, 2d & 2f. The initial Ni 2p$_{3/2}$ spectra and its satellite peak at higher binding energy was deconvoluted to show contributions from metallic nickel at 852.61 eV, Ni(OH)$_2$ at 855.91 and 861.91 eV and Ni$_2$O$_3$ at 855.61 and 861.76 eV. This is generally similar to what has been recorded in literature [8,11,16].

After potential cycling the majority of the spectra originates from Ni (OH)$_2$ at 855.62 and 861.47 eV, with weak contributions from metallic nickel at 852.02 eV, NiO at 854.12, 857.42 and 862.37 eV and NiOOH at 856.67 eV. The pristine iron 2p$_{3/2}$ spectra and its satellite peak were deconvoluted to metallic iron at 706.81 eV, FeO at 711.01 eV, Fe$_2$O$_3$ at 711.01 eV and FeOOH at 712.21 and 714.01 eV. The post-potential cycling spectra displays an increase in FeOOH and a corresponding decline in FeO. The spectra was deconvoluted to metallic iron at 706.82 eV, FeO at 711.02 eV, Fe$_2$O$_3$ at 711.17 eV and FeOOH at 712.22 eV. These peaks are also in accordance with literature [15,16], though the intensity of metallic Fe in the pristine sample appears variable when comparing both literature and the currently presented work [13,15], however this might be attributed to the production process of the stainless steel felt.

The pristine chromium 2p$_{3/2}$ spectra was deconvoluted to show chromium metal at 573.71 eV, chromium(III) oxide at 575.51, 576.41 and 578.06 eV, chromium(III) hydroxide at 577.46 eV and chromium (IV) oxide at 579.56 eV. The cycled sample shows the same species, metallic chromium at 573.71 eV, chromium(III) oxide at 575.82 and 576.57 eV, chromium(III) hydroxide at 577.62 eV, chromium(IV) oxide at 579.42 eV and chromium(IV) hydroxide at 579.57 eV. A significant increment in chromium(III) hydroxide is clear, in addition to a generally improved signal. The Cr 2p$_{3/2}$ spectra is less frequently displayed in related literature due to its disappearance after anodic corrosion, though the peaks are within the reported range [15,16].

The general decline in Ni 2p$_{3/2}$ binding energy after potential cycling corresponds to the decline in oxidation state from Ni(III) to Ni(II), which correlates to the behaviour predicted by a nickel Pourbaix diagram [17] The increase in Cr 2p$_{3/2}$ binding energies are due to the general increase in oxidation state as there is a greater influence of Cr(IV) compared against the pristine sample. While the Fe 2p$_{3/2}$ binding energies are
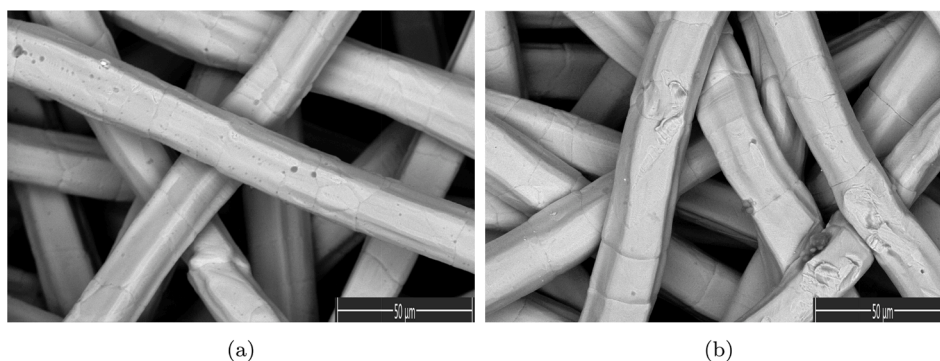

(a)   (b)

Fig. 1. SEM figures **(a)** before and **(b)** after potential cycling thereby showcasing the physical surface effects of the process.

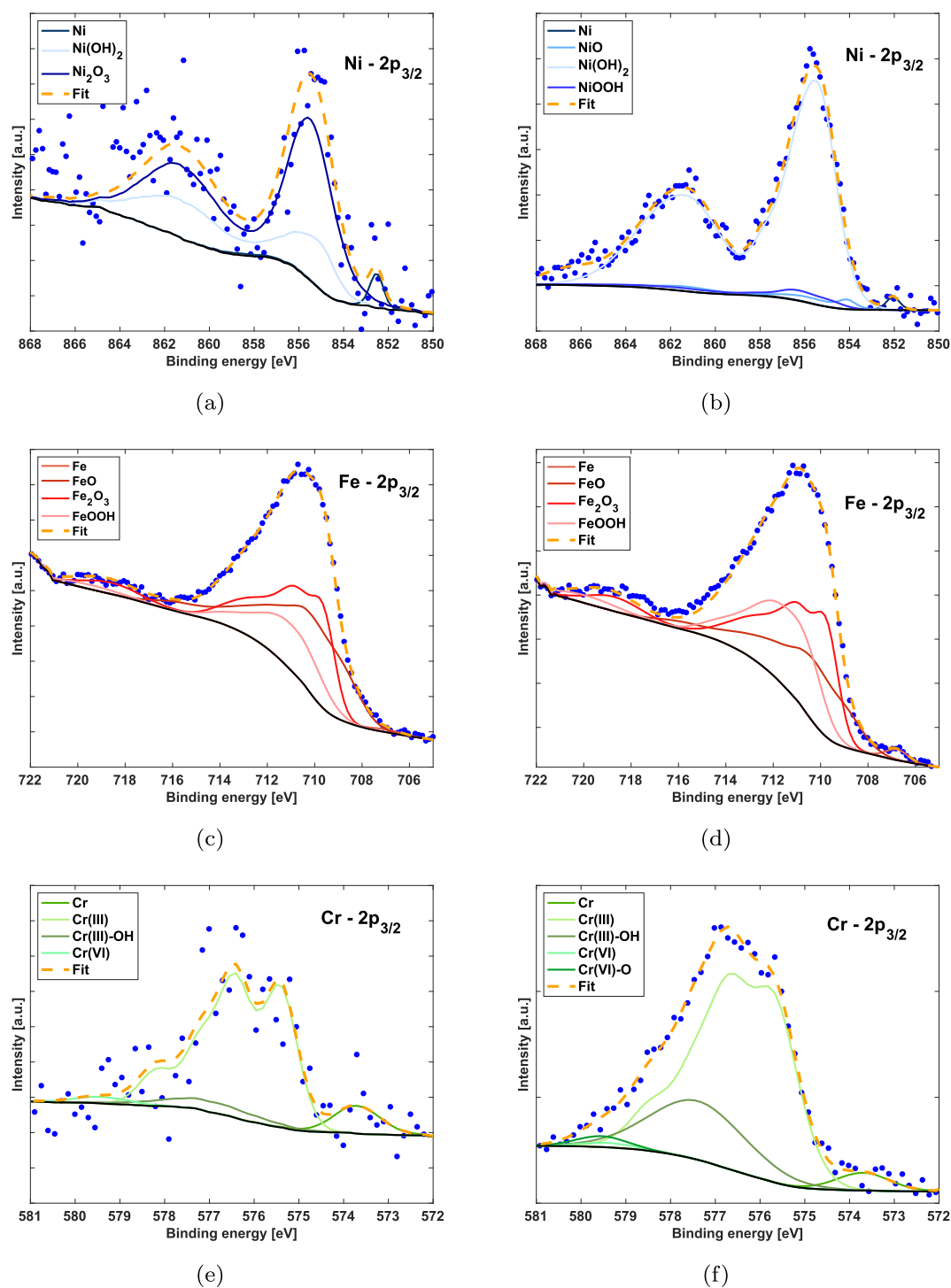**Fig. 2.** High-resolution XPS-spectra of the **(a)** & **(b)** nickel $2p_{3/2}$ spectra, **(c)** & **(d)** the iron $2p_{3/2}$ spectra and **(e)** & **(f)** the chromium $2p_{3/2}$ spectra before and after potential cycling.

remarkably similar, there is evidence of a greater influence of a higher oxidation states (Fe(III)) after potential cycling, also in accordance with the iron Pourbaix diagram [17].

XRD spectra were collected before and after potential cycling in a Bragg–Brentano configuration between 30–120°C as shown in Fig. 3a. The pristine and cycled samples yielded lattice parameters of 3.5923(4) Å and 3.5925(6) Å respectively. The pristine SSF displays XRD peaks corresponding to 316L stainless steel [15,18]. Strong peaks at 43.66°, 50.85°, 74.73°, 90.71°, 95.97° and 118.16° attributed to the 111, 200, 220, 311, 222 and 310 planes of austenitic stainless steel [15,18,19].

The pristine sample shows strong characteristics of an FCC-type austenitic (ICDD 33–0397) structure without the impurities of BCC (ICDD 34–0396) structures traditionally reported for such alloys [18,20]. The same peaks were displayed by the cycled sample, however a slight shift towards lower angles is noted in addition to a change in peak shape and their relative intensities. The shift is likely associated with the varying height in the samples. The change in peak shape is either due to domain-size effects or microstrain, where differentiating between these two effects can be challenging. Inclusion of microstrain effects in fitting the data yield average domain sizes of 104 nm and 103
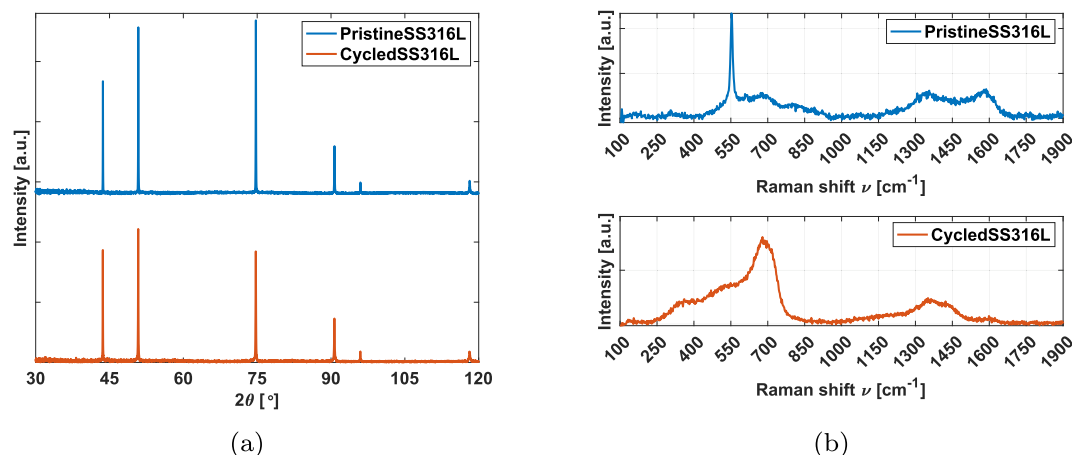
Fig. 3. **(a)** XRD spectra and **(b)** Raman spectra collected before and after potential cycling.

nm for the pristine and cycled samples. This amounts to notably greater influence from microstrain relative to the pristine sample (x300), where the combination of this increase in microstrain and decline in domain size has been associated with increased resistance to uniform corrosion, albeit an increase in the likelihood of pitting corrosion [21]. The small decline in domain size has been associated with increased corrosion resistance associated with a passive film rich in $Ni(OH)_2$, thereby corroborating the XPS-determined surface composition [22,23].

Raman spectra were collected as displayed in Fig. 3b, where the pristine sample displays very similar peaks and peak intensities to that reported by Zamanizadeh *et* al. [8] for a similar 316L electrode. Peaks at 285 (Fe_2O_3), 552 (Cr_2O_3), 587 (NiO), 689 (Fe_3O_4), 804 (Fe_3O_4) and 1370 cm^{-1} (Fe_3O_4) [8,24,25]. The cycled sample exhibits a radically different spectra, presenting peaks at 156 (α-Fe_2O_3), 346 (Cr_2O_3), 567 ($Ni(OH)_2$), 691 (γ-FeOOH), 1299 (γ-FeOOH), 1359 (δ-FeOH), 1440 (γ-FeOOH) and 1604 cm^{-1} (Fe_3O_4) [8,24,25]. These peaks confirm several of the XPS-determined oxidation states. The electrode composition was analysed with several physicochemical methods to reveal the surface and the bulk composition. Table 1 exhibits that the surface composition of chromium and nickel increases at the cost of iron after potential cycling. EDS data shows that the atomic content of chromium increases, however nickel decreases together with iron indicating that the bulk concentration of nickel decreases as it migrates to the surface during PC, where these phenomena coincide with the diffusion rate of both iron and nickel within an alloy [26,27]. This corresponds with established literature where the oxidation of iron and chromium proceeds that of nickel [28], which corresponds with the XPS results. Additional details on the oxidation states of each element before and after PC are shown in Tab. S1-S3.

3.2. Electrochemical analysis

3.2.1. Three-electrode measurements

The performance of the 316L stainless steel electrode was tested before and after the potential cycling according to the experimental protocol specified in the supplemental material. The full range voltammograms depicted in Fig. 4a show the Fe(II)/Fe(III) redox couple ((1) & (2)), followed by the Ni(II)/Ni(III) redox couple ((3) & (5)) succeeded by the OER (4) [29,30]. The oxidising/reducing peaks of iron increase/decrease, corresponding to an increase in the oxide layer and a general increase in oxidation state. The nickel redox couple shows a slight different trend, where the oxidising peak decreases rapidly while the reducing peak undergoes a slightly increment. The peaks around + 0.60/0.50 $E_{Ag/AgCl}$ are likely two peaks, the second originating from the Cr(III)/Cr(VI) redox couple [8]. Overall, the trends in Fig. 4a mostly adhere to established trends in literature [8,31].

A slight divergence from the aforementioned trends is that the upper layer of the surface predominantly comprised iron based off the XPS-determined surface composition shown in Fig. 2. The chromium and nickel portion increases notably after PC, while the iron content undergoes 28.2% reduction. Based off the XPS results, it would appear that the formation of a corrosion-resistant layer appears after the initial decline of the surface layer of iron following the 1000 cycles, yielding a layer with the approximate composition of $CrFe_5Ni_2$-O_xH_y. The CV scans in Fig. 4b show the gradual decline in activity of the Ni(II)/Ni(III) redox couple [13] as the number of scans increase. Moreover, no catalytic activity of the other components of 316L stainless steel were active during the investigated potential region which corresponds to previously reported literature [13].

In addition, the charge of the oxidising/reducing peaks was determined and plotted as a function of scan number in Fig. 4c, where the anode charge shows a slight decline, however the charge affiliated with the reducing peak declined notably. This is evidence of the formation of an oxide layer, which correlates with post-potential cycling XPS results where the metal XPS-spectra can be almost exclusively attributed to hydroxides/oxides as shown in Tab. S1-S3. This is also seen in the oxygen 1s spectra in Fig. S3, where the same hydroxide bonds are seen from the oxygen 1s perspective. A 9.35% increase in the electrochemical active surface area was identified due to potential cycling, as shown in Fig. S4.

Fig. 4d shows LSV curves before and after PC, where the SSF porous transport layer (PTL) clearly shows increased activity after PC, despite the gradual decline in charge associated with the cycled redox couple shown in Fig. 4b. The performance of the SSF was compared with Solid SS316L sample as indicated. Increased concentration of surface-adjacent chromium and nickel content has previously been shown to increase OER activity [8,32,33].

The electrochemical impedance spectroscopy (EIS) spectra in Fig. 4d–4e & S4 showcases the notable improvement in performance as the polarisation resistance declines $\approx$68% at the creation of the $CrFe_5Ni_2$-O_xH_y layer. Similar CrFeNiO materials have been shown

Table 1
XPS- and EDS-determined compositions of the stainless steel electrode before and after potential cycling.

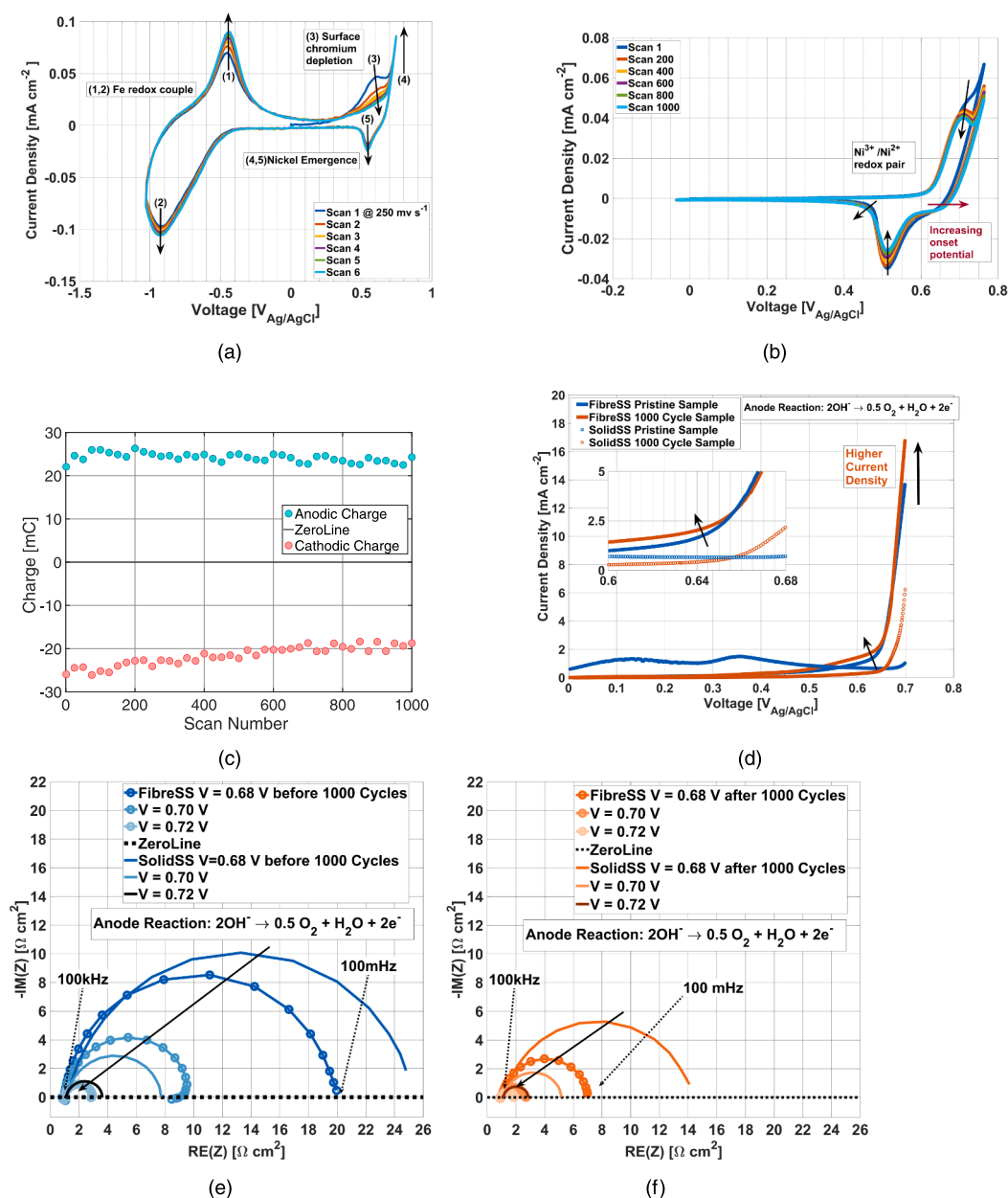|	State			
XPS		Cr - 2p$_{3/2}$ [at.%]	Fe - 2p$_{3/2}$ [at.%]	Ni - 2p$_{3/2}$ [at.%]
	Pristine	3.676	87.33	8.997
	Cycled	12.54	62.73	24.73
EDS		Cr [at.%]	Fe [at.%]	Ni [at.%]
	Pristine	21.46	63.95	8.643
	Cycled	21.89	62.93	7.870

Fig. 4. (a) The cyclic voltammetry scan of the SSF porous transport layer (PTL) at 250 mV s^{-1} between - 1.036 to + 0.70 V versus $E_{Ag/AgCl}$ reference electrode. **(b)** The 1000 cycle voltammogram trend.**(c)** The anodic and cathodic charges calculated for the $Ni^{2+/3+}$ redox couple peaks. **(d)** The linear sweep voltammetry (LSV) performed between 0 to + 0.70 V ($E_{Ag/AgCl}$) shows a higher current density for the 1000 cycle sample. The EIS spectra of the SSF PTL **(e)** before and **(f)** after cycling, at three potentials of 0.68, 0.70 and 0.72 V ($E_{Ag/AgCl}$) respectively.

catalytic activity towards the OER [32–34]. While a great decline in polarisation resistance is evident, there was also a slight increase in series resistance as seen in Fig. S5. The great decline in polarisation resistance is rationalised by the large increase of FeOOH and Ni(OH)$_2$ after PC, as seen in the XPS analysis. The combination of even trace amounts of Fe was shown to notably increase the OER activity of Ni (OH)$_2$ films [35].

3.2.2. Single cell AEMWE measurements

After characterising the microstructure and analysing the three-electrode performance of the SSF PTLs, a single cell anion exchange membrane electrolyser was assembled and tested at 25$°C$ in 1.0 M KOH for water splitting reaction as shown in Eq. 1.

$$H_2O(l) \longrightarrow H_2(g) + \frac{1}{2}O_2(g) \tag{1}$$

The performance of the single cell AEMWE with the cycled SSF had increased by 7.2% compared to pristine SSF as shown in Fig. 5a. The origin of this increment can predominantly be attributed to improved kinetics as seen by the iR-corrected LSV curves. The corresponding EIS data at 0 V showed a relatively higher impedance trend at lower frequencies for the cycled sample, suggesting an adverse diffusion effect of CrFe$_5$Ni$_2$-O$_x$H$_y$ layer growth on OER, as shown in Fig. 5b–5c.

Consequently, additional EIS measurements were performed at the onset of OER overpotential, as shown in Fig. 5c. The raw EIS data were corrected for inductance and smoothened using DRTTools [36] to clearly analyse the spectra. The EIS spectra revealed 31% lower series resistance for the cycled SSF compared to the Pristine SSF when tested in a full cell, as shown in Fig. 5d. In addition, the total impedance was 29% higher, largely due to diffusion effects at lower frequencies upon the formation of a CrFe$_5$Ni$_2$-O$_x$H$_y$ layer [37].
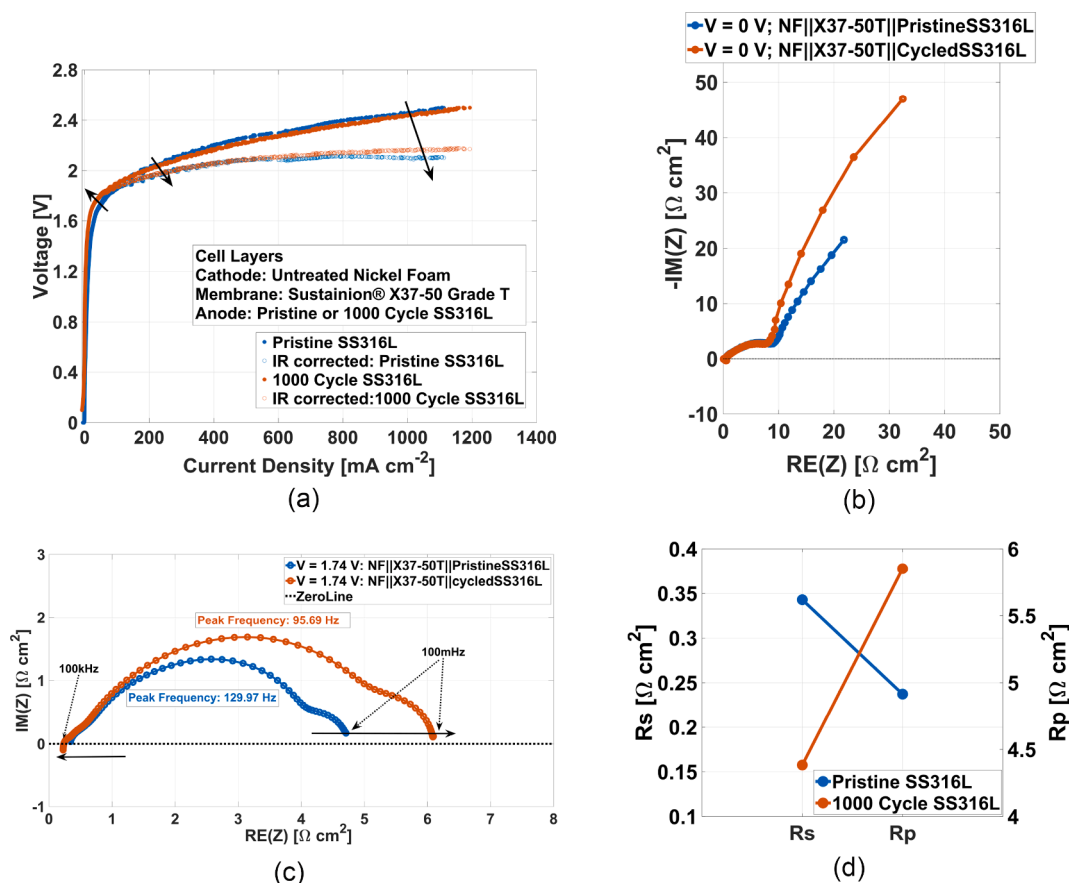
Fig. 5. The full cell performance comparison between the pristine SSF (blue) and cycled SSF (red) at 25 °C, 1.0 M KOH. **(a)** The original and 90% iR-corrected LSV curves. **(b)** Open circuit (0 V) potentiostatic EIS spectra with 5.0 mV amplitude. **(c)** The potentiostatic EIS spectra at 1.74 V with 5 mV amplitude to probe OER onset region. **(d)** The corresponding change in the series (R_s) and polarisation resistances (R_p).

4. Conclusion

The use of 316L stainless steel felt (SSF) has great application potential as a porous transport layer (PTL) in alkaline-based electrolysers. This paper details the effects of ex-situ potential cycling a SSF PTL in 1.0 M KOH, and the impact of utilising a PTL with this pretreatment in an anion exchange membrane water electrolysis cell. After 1000 potential cycles, the surface composition of the SSF changed with a clear increase in chromium and nickel content at the expense of iron. This is explained through the diffusion coefficients of the respective elements in the alloy. Improvement in kinetic efficiency was related to surface conditions through the formation of a $CrFe_5Ni_2$-O_xH_y layer as determined by XPS and supported by XRD and Raman spectra, yielding an ≈68% reduction in polarisation resistance. This single cell anion exchange membrane electrolyser performance increased by 7.2% at 2.5 V with cycled SSF PTL reaching a current density of 1193 mA cm^{-2} at 25°C.

Declaration of Competing Interest

The authors declare that they have no known competing financial interests or personal relationships that could have appeared to influence the work reported in this paper.

Acknowledgements

The authors would like to thank Dr. Mounir Mensi, Dr. Emmanuelle Boehm Courjault and Dr. Pascal Schouwink at EPFL for their expertise, high quality and efficiency of XPS, SEM and XRD analysis respectively. The authors would also like to warmly acknowledge the expertise of Mr.

Appendix A. Supplementary material

Supplementary data associated with this article can be found, in the online version, at https://doi.org/10.1016/j.elecom.2022.107418.

References

[1] N. Du, C. Roy, R. Peach, M. Turnbull, S. Thiele, C. Bock, Anion-exchange membrane water electrolyzers, Chem. Rev. 122 (13) (2022) 11830–11895.
[2] T.B. Ferriday, P.H. Middleton, 4.07 - Alkaline Fuel Cells, Theory and Applications, in: T.M. Letcher (Ed.), Comprehensive Renewable Energy (Second Edition), second edition, Elsevier, Oxford, 2022, pp. 166–231.
[3] P. Shirvanian, A. Loh, S. Sluijter, X. Li, Novel components in anion exchange membrane water electrolyzers (AEMWE–s): Status, challenges and future needs, A mini review, Electrochemistry Communications 132 (2021) 107140.
[4] T. Ferriday, P. Middleton, Alkaline fuel cell technology - A review, Int. J. Hydrogen Energy 46 (35) (2021) 18489–18510.
[5] J. Yang, M. Jang, X. Zeng, Y. Park, J. Lee, S. Choi, Y. Yin, Non-precious electrocatalysts for oxygen evolution reaction in anion exchange membrane water electrolysis: A mini review, Electrochem. Commun. 131 (2021) 107118.
[6] H. Ito, N. Miyazaki, S. Sugiyama, M. Ishida, Y. Nakamura, S. Iwasaki, Y. Hasegawa, A. Nakano, Investigations on electrode configurations for anion exchange membrane electrolysis, J. Appl. Electrochem. 48 (3) (2018) 305–316.
[7] F. Moureaux, P. Stevens, G. Toussaint, M. Chatenet, Timely-activated 316L stainless steel: A low cost, durable and active electrode for oxygen evolution reaction in concentrated alkaline environments, Applied Catalysis B: Environmental 258 (2019) 117963.
[8] H. Zamanizadeh, S. Sunde, B. Pollet, F. Seland, Tailoring the oxide surface composition of stainless steel for improved OER performance in alkaline water electrolysis, Electrochim. Acta 140561 (2022).

[9] S. Anantharaj, H. Sugime, S. Noda, Surface amorphized nickel hydroxy sulphide for efficient hydrogen evolution reaction in alkaline medium, Chem. Eng. J. 408 (2021) 127275.

[10] M. Lavorante, J. Franco, Performance of stainless steel 316L electrodes with modified surface to be use in alkaline water electrolyzers, Int. J. Hydrogen Energy 41 (23) (2016) 9731–9737.

[11] N. Todoroki, T. Wadayama, Electrochemical stability of stainless-steel-made anode for alkaline water electrolysis: Surface catalyst nanostructures and oxygen evolution overpotentials under applying potential cycle loading, Electrochem. Commun. 122 (2021) 106902.

[12] F. Moranchell, J. Pineda, J. Pérez, U. Silva-Rivera, C. Escobedo, R. Huerta, Electrodes modified with Ni electrodeposition decrease hexavalent chromium generation in an alkaline electrolysis process, Int. J. Hydrogen Energy 45 (26) (2020) 13683–13692.

[13] F. Yu, F. Li, L. Sun, Stainless steel as an efficient electrocatalyst for water oxidation in alkaline solution, Int. J. Hydrogen Energy 41 (10) (2016) 5230–5233.

[14] F. Le Formal, L. Yerly, E. Potapova Mensi, X. Pereira Da Costa, F. Boudoire, N. Guijarro, A. Zuttel, K. Sivula, Influence of Composition on Performance in Metallic Iron–Nickel–Cobalt Ternary Anodes for Alkaline Water Electrolysis, ACS Catalysis 10 (20) (2020) 12139–12147.

[15] S. Anantharaj, M. Venkatesh, A. Salunke, T. Simha, V. Prabu, S. Kundu, High-performance oxygen evolution anode from stainless steel via controlled surface oxidation and cr removal, ACS Sustainable Chemistry & Engineering 5 (11) (2017) 10072–10083.

[16] J. Chastain, R. King Jr, Handbook of X-ray photoelectron spectroscopy, Perkin-Elmer Corporation 40 (1992) 221.

[17] B. Beverskog, I. Puigdomenech, Pourbaix diagrams for the ternary system of iron-chromium-nickel, Corrosion 55 (11) (1999) 1077–1087.

[18] F. Weng, S. Gao, J. Jiang, J. Wang, P. Guo, A novel strategy to fabricate thin 316L stainless steel rods by continuous directed energy deposition in Z direction, Additive Manufacturing 27 (2019) 474–481.

[19] A. Forgas Júnior, J. Otubo, R. Magnabosco, Ferrite quantification methodologies for duplex stainless steel, Journal of Aerospace Technology and Management 8 (2016) 357–362.

[20] J. Slotwinski, E. Garboczi, P. Stutzman, C. Ferraris, S. Watson, M. Peltz, Characterization of Metal Powders Used for Additive Manufacturing, Journal of research of the National Institute of Standards and Technology 119 (2014) 460.

[21] D. Sprouster, W. Cunningham, G. Halada, H. Yan, A. Pattammattel, X. Huang, D. Olds, M. Tilton, Y. Chu, E. Dooryhee, et al., Dislocation microstructure and its influence on corrosion behavior in laser additively manufactured 316L stainless steel, Additive Manufacturing 47 (2021) 102263.

[22] L. Wang, J. Zhang, Y. Gao, Q. Xue, L. Hu, T. Xu, Grain size effect in corrosion behavior of electrodeposited nanocrystalline Ni coatings in alkaline solution, Scripta Mater. 55 (7) (2006) 657–660.

[23] S. Sabooni, H. Rashtchi, A. Eslami, F. Karimzadeh, M. Enayati, K. Raeissi, A. Ngan, R. Imani, Dependence of corrosion properties of AISI 304L stainless steel on the austenite grain size, Int. J. Mater. Res. 108 (7) (2017) 552–559.

[24] P. Colomban, Potential and drawbacks of Raman (micro) spectrometry for the understanding of iron and steel corrosion, INTECH Open Access Publisher (2011).

[25] M. Aghazadeh, H. Rad, In situ growth of Ni(OH)$_2$-porous nitrogen-doped graphene composite onto Ni foam support as advanced electrochemical supercapacitors materials, J. Mater. Sci.: Mater. Electron. 33 (14) (2022) 11038–11054.

[26] J. Huang, X. Wu, E.-H. Han, Electrochemical properties and growth mechanism of passive films on Alloy 690 in high-temperature alkaline environments, Corros. Sci. 52 (10) (2010) 3444–3452.

[27] K. Shimizu, H. Habazaki, P. Skeldon, G. Thompson, G. Wood, GDOES depth profiling analysis of the air-formed oxide film on a sputter-deposited Type 304 stainless steel, Surface and Interface Analysis: An International Journal devoted to the development and application of techniques for the analysis of surfaces, interfaces and thin films 29 (11) (2000) 743–746.

[28] C.-O. Olsson, D. Landolt, Passive films on stainless steels–chemistry, structure and growth, Electrochim. Acta 48 (9) (2003) 1093–1104.

[29] D. Hall, C. Bock, B. MacDougall, The Electrochemistry of Metallic Nickel: Oxides, Hydroxides, Hydrides and Alkaline Hydrogen Evolution, Journal of The Electrochemical Society 160 (3) (2013) F235.

[30] D. Hall, An Electrochemical and Spectroscopic Investigation of Nickel Electrodes in Alkaline Media for Applications in Electro-Catalysis, Ph.D. thesis, Université d'Ottawa/University of Ottawa, 2014.

[31] C. Abreu, M. Cristóbal, R. Losada, X. Nóvoa, G. Pena, M. Pérez, The effect of Ni in the electrochemical properties of oxide layers grown on stainless steels, Electrochim. Acta 51 (15) (2006) 2991–3000.

[32] R. Singh, J. Singh, B. Lal, M. Thomas, S. Bera, New NiFe$_{2-x}$Cr$_x$O$_4$ spinel films for O$_2$ evolution in alkaline solutions, Electrochim. Acta 51 (25) (2006) 5515–5523.

[33] D. Zhang, Z. Yang, Y. Yang, H. Li, X. Wang, Highly active hollow mesoporous NiFeCr hydroxide as an electrode material for the oxygen evolution reaction and a redox capacitor, Chem. Commun. 56 (99) (2020) 15549–15552.

[34] X. Bo, Y. Li, R. Hocking, C. Zhao, NiFeCr Hydroxide Holey Nanosheet as Advanced Electrocatalyst for Water Oxidation, ACS Appl. Mater. Interfaces 9 (47) (2017) 41239–41245.

[35] L. Trotochaud, S. Young, J. Ranney, S. Boettcher, Nickel–Iron Oxyhydroxide Oxygen-Evolution Electrocatalysts: The Role of Intentional and Incidental Iron Incorporation, J. Am. Chem. Soc. 136 (18) (2014) 6744–6753.

[36] T. Wan, M. Saccoccio, C. Chen, F. Ciucci, Influence of the Discretization Methods on the Distribution of Relaxation Times Deconvolution: Implementing Radial Basis Functions with DRTtools, Electrochim. Acta 184 (2015) 483–499.

[37] I. Vincent, E.-C. Lee, H.-M. Kim, Comprehensive impedance investigation of low-cost anion exchange membrane electrolysis for large-scale hydrogen production, Scient. Rep., Nature Publishing Group 11 (1) (2021) 1–12.